IFC-CNR / TESRE-CNR /
UNIMI / LABEN / JPL / OAT
LFI Project System Team

Planck LFI

TITLE: **Effect of Sorption Cooler Temperature Variations on LFI Front-End**

DOC. TYPE: TECHNICAL NOTE

PROJECT REF.: PL-LFI-PST-TN-005 **PAGE:** I of IV, 30

ISSUE/REV.: 2.0 **DATE:** October 2001

Prepared by	A. Mennella M. Bersanelli R. Ferretti G. Morgante M. Prina C. Burigana D. Maino LFI Project System Team	Date: Signatures:	October 16th, 2000
Agreed by	C. BUTLER LFI Program Manager	Date: Signature:	October 16th, 2000
Approved by	N. MANDOLESI LFI Principal Investigator	Date: Signature:	October 16th, 2000

DISTRIBUTION LIST

Recipient	Company / Institute	E-mail address	Sent
E. ALIPPI	LABEN – Vimodrone	alippi.e@laben.it	Yes
E. ARTAL	Univ. of Cantabria – Santander	artal@dicom.unican.es	Yes
M. BERSANELLI	IFCTR – Milano	marco@ifctr.mi.cnr.it	Yes
C. BUTLER	TESRE – Bologna	butler@tesre.bo.cnr.it	Yes
C. BURIGANA	TESRE – Bologna	burigana@tesre.bo.cnr.it	Yes
B. COLLAUDIN	ASPI – Cannes	Bernard.Collaudin@space.alcatel.fr	Yes
R. DAVIS	JBO – UK	rjd@jb.man.ac.uk	Yes
R. EMERY	RAL – Chilton (UK)	R.J.Emery@rl.ac.uk	Yes
R. FERRETTI	LABEN – Vimodrone	ferretti.r@laben.it	Yes
T. GAIER	JPL – Pasadena	gaier@merlin.jpl.nasa.gov	Yes
R. HOYLAND	LABEN – Milano	rjh@ll.iac.es	Yes
C. LAWRENCE	JPL – Pasadena	crl@jplsp.jpl.nasa.gov	Yes
D. MAINO	OAT – Trieste	maino@ts.astro.it	Yes
N. MANDOLESI	TESRE – Bologna	reno@tesre.bo.cnr.it	Yes
A. MENNELLA	IFC – Milano	daniele@ifctr.mi.cnr.it	Yes
G. MORGANTE	JPL – Pasadena	gianluca@squid.jpl.nasa.gov	Yes
F. PASIAN	OAT – Trieste	pasian@oat.ts.astro.it	Yes
T. PASSVOGEL	ESA – PT	tpassvog@estec.esa.nl	Yes
M. PRINA	JPL – Pasadena	mauro@squid.jpl.nasa.gov	Yes
M. SEIFFERT	JPL – Pasadena	Michael.d.seiffert@jpl.nasa.gov	Yes
J. TAUBER	ESA	jtauber@astro.estec.esa.nl	Yes
J. TUOVINEN	Millilab – Finland	Jussi.tuovinen@vtt.fi	Yes
F. VILLA	TESRE – Bologna	villa@tesre.bo.cnr.it	Yes
L. WADE	JPL – Pasadena	lawrence.a.wade@jpl.nasa.gov	Yes
LFI System PCC	TESRE – Bologna	lfispcc@tesre.bo.cnr.it	Yes
Radiometer WG		rwg@beta.jpl.nasa.gov	Yes

CHANGE RECORD

Issue	Date	Sheet	Description of Change	Release
Draft 0.1	February ‘00	All	First issue draft of document	
Draft 0.2	March ‘00	All	Second issue draft of document, general updating	
Issue 1.0	April '00	All	First issue of document	
Issue 1.1	June '00	All	Second issue of document. Corrections in equation (8) and (9)	
Issue 2.0	October '01	All	Third issue of document. General updating, considering JPL simulations of sorption cooler temperature fluctuations	

TABLE OF CONTENTS

Abstract

In this technical note we provide a major update of the analysis of impact of front-end thermal fluctuation on LFI measurements. In this update we consider JPL latest simulations concerning the stability of the Sorption Cooler Cold End, the thermal damping provided by the LFI mechanical structure and the partial removal of the final systematic effect from the LFI maps obtained using a so-called "destriping" algorithm. Our results indicate that although several factors contribute to reduce the impact of Sorption Cooler thermal instabilities on the measured sky signal, the final systematic effect cannot be considered negligible, especially if the Sorption Cooler will not work under ideal conditions.

1 Introduction

In this document we discuss the impact of front-end thermal fluctuations on LFI measurements. A reissue of this technical note has been prompted by several novel results since the last issue [1], in particular:

- simulations run at JPL have provided a more realistic picture of the **shape of temperature oscillations** at the Sorption Cooler Cold End (SCCE);
- a more refined thermal modelling of LFI has better defined the **damping of thermal oscillations** from the SCCE to the radiometers due to the LFI mechanical structure [2];
- a first analysis of systematic errors in PLANCK-LFI has provided **requirements on the maximum acceptable systematic caused by front-end thermal instabilities** [3];
- an analysis of the application of destriping algorithms to the Time Ordered Data has given estimates to the **ability to remove** such periodic signals from the measured data.

This note is structured according to the following sections:

- in section 2 we present LFI current requirements on the maximum acceptable systematic errors induced by front-end temperature instabilities as discussed in [3];
- in section 3 we present and discuss results from recent simulations of the SCCE behaviour, highlighting the effect of non-ideal behaviours in the Sorption Cooler compressor assembly on temperature stability;
- in section 4 we present results from LFI thermal model showing the damping of temperature fluctuations caused by the LFI mechanical structure. In this section we also estimate the expected temperature oscillation curve at the LFI front-end level (feed-OMT and FEMs);
- in section 5 we derive the instrument transfer function for front-end temperature oscillations and discuss the sensitivity of the radiometers to physical temperature variations;
- in section 6 we present the results of this analysis showing maps of the spurious signal induced by front-end temperature fluctuations. We also provide some estimates of the ability to reduce the level of this systematic error by applying destriping algorithms to the Time Ordered Data;
- in section 7 we summarise the results comparing them to the requirements detailed in section 2 and provide some recommendations for future actions.

2 Requirements on maximum systematic errors induced by front-end temperature fluctuations

A fundamental requirement for Planck is a strict control of systematic errors that must be kept at μK level in the final maps. A definition of systematic error is given in [3]:

"Systematic error" is any process that leads to (i) a measurement of a point on the sky that is different than its true value, or to (ii) a degradation of the instrument angular resolution[1]*.*

In the same document the requirement on the total acceptable systematic error level is defined:

LFI-INS-8	The global contribution from all systematic effects in a pixel at the end of mission will not contribute more than ±3 μK (6 μK peak-to-peak) (TBC).

In general systematic errors can be divided into two broad categories according to their frequency compared to the spacecraft spin frequency, i.e.:

- spurious signals that vary synchronously with the spacecraft spin (i.e. signals which are characterised by a frequency ν_f such that $k\,\nu_f = \nu_{spin}$, with k integer). These signals come naturally from external celestial sources, but can also be generated "internally" in the spacecraft (an example is represented by spin synchronous harmonics of thermal fluctuations). Although some data analysis methods have been developed to deal with this kind of systematic effects they may be particularly critical to remove from the data stream because of their similarity with the *true* sky signal;
- other periodic (non-spin synchronous) fluctuations. In this case after a time interval Δt during which the same pixel is measured every 60 seconds (the spin period) the signal oscillation is damped by a factor of approximately $1/(2\pi\nu_f \Delta t)$. A further reduction in the level of this kind of systematic errors can be obtained by applying destriping algorithms to the Time Ordered Data. In the case of signal fluctuations induced by the Sorption Cooler, the main non spin synchronous frequencies will be 1/667 Hz (which is the frequency of each compressor bed) and 1/4000 Hz (which corresponds to the frequency of the whole compressor assembly).

A specific requirement on the maximum systematic error caused by spin-synchronous effects is stated as follows:

LFI-INS-10	The global contribution from spin synchronous fluctuations in each pixel will be less than ±2 μK (4 μK peak-to-peak). This includes spin synchronous harmonics of lower frequency periodic effects.

In Table 2-1 (taken from [3]) we report the LFI error budget relative to systematic errors caused by thermal fluctuations; in bold font we highlight the values relative to the front-end (feed-OMT + FEMs).

Table 2-1 – Breakdown of LFI error budget caused by thermal fluctuations

Source	Error from spin synch. fluct. (μK)	Error from other periodic fluct. (μK)
Front-End	**± 0.45**	**± 0.9**

[1] Note that this definition of "systematic error", for example, does not include the residual error in removing foregrounds which contribute to the main beam, while it does include foregrounds contribution through the side-lobes.

Waveguides	± 0.4	± 0.4
BEMs	± 0.4	± 0.4
DAE	± 0.4	± 0.4
Total	***± 0.8***	***± 1.1***

The values listed in Table 2-1 represent the maximum error that can be tolerated in the final maps after destriping; in our analysis we will calculate what level of systematic error is expected considering our current understanding of the Sorption Cooler behaviour.

3 Temperature oscillations at the SCCE

3.1 The Sorption Cooler System

The sorption cooler is a cooling machine that performs a Joule-Thomson (J-T) cycle using hydrogen as the working fluid. The key element of the whole cooler system is the compressor, an absorption machine able to pump hydrogen gas by thermally cycling several sorbent compressor units on the basis of a process known as *chemi-sorption*, indicating the chemical nature of the absorbing-desorbing processes. A schematic of this system is shown in Figure 3-1.

The major advantage of this solution is the absence of moving parts (except for the check valves diaphragms), so that the cooler can be considered virtually vibration-free. The principle of operation of the sorption compressor is based on an unique sorption material ($La_{1.0}Ni_{4.78}Sn_{0.22}$) which can absorb large amounts of hydrogen gas at relatively low pressures and then, when heated in a limited volume, can desorb the gas to produce high-pressure hydrogen. Heating of the sorbent is accomplished by electrical resistance heaters, while its cooling is achieved by thermally connecting the compressor element to a radiator at 270 K.

The system is periodically cycled between heating and cooling phases, producing high-pressure gas intermittently. In order not to loose excessive amounts of power during heating, a heat switch is provided to alternately isolate the sorbent bed from the radiator during the heating phase and to thermally connect to it during the cooling phase.

Each sorption compressor element (i.e. sorbent bed) is characterised by a cycle of four steps: heat up, desorption, cool down, absorption. This implies an intermittent intake of low pressure hydrogen and output of high-pressure hydrogen. If the high-pressure hydrogen is pre-cooled with radiators to below the inversion temperature and then expanded through a Joule-Thomson expansion orifice (J-T) the high-pressure gas will partially liquefy, producing liquid refrigerant at low pressure collected into reservoirs for the intended load. Heat dissipated by the thermal load on the cold head evaporates the liquid and the low-pressure gaseous hydrogen is re-circulated back to the cool sorbent beds for compression. In order to produce a continuous, and approximately constant, stream of liquid refrigerant, several identical sorption beds are needed to stagger their phases so that at any given time, one is hot and desorbing gas while the others are either heating, cooling, or re-absorbing low pressure gas.

In such a system, there is a basic clock time period over which each step of the process is conducted: the duration of each phase is 667 s, so that the six compressor elements are cycled successively through the steps in the process with one complete cycle taking as baseline 4000 s.

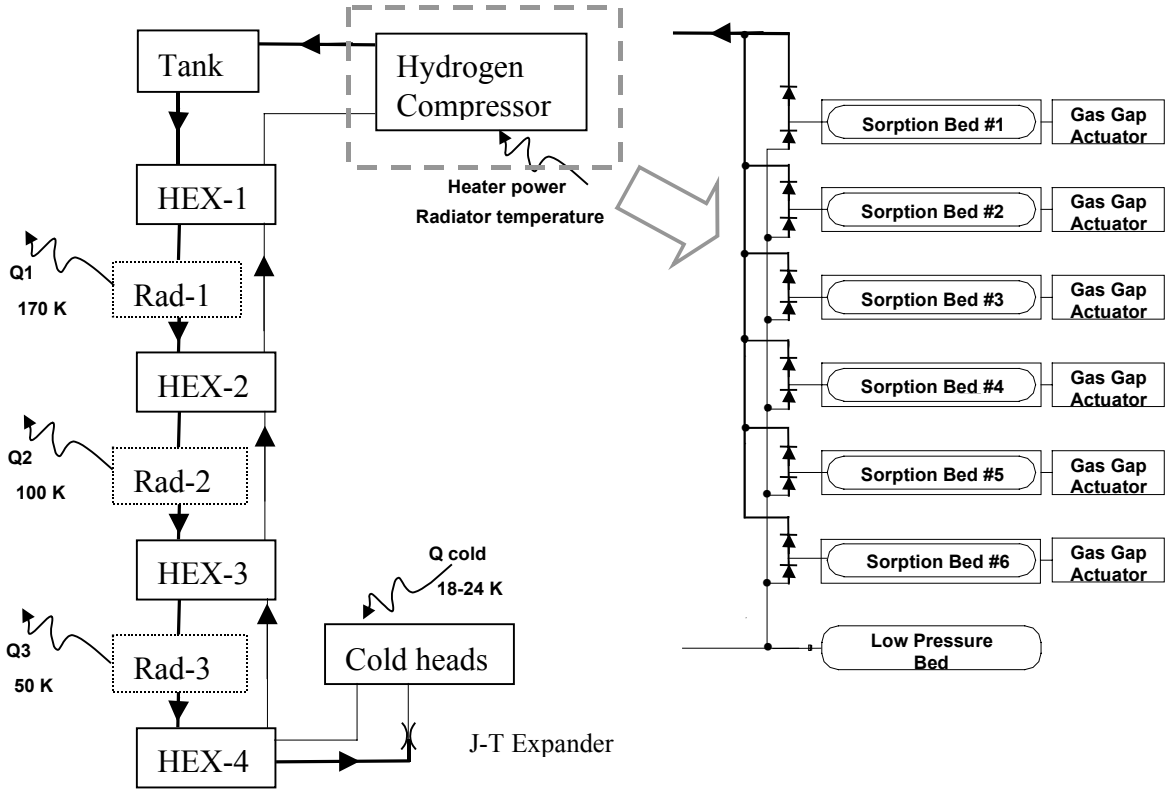

Figure 3-1. Planck sorption cooler schematic, with the three pre-cooling radiators, four heat exchangers, the cold heads and the compressor. The arrows in front of each bed sorption bed are check valves, allowing flow only in the arrow direction.

3.2 Sources of temperature fluctuations in the Sorption Cooler

In principle we could say that almost every sorption cooler subsystem affects the cold-head temperature stability: the hydride non-linear characteristic, the timing of the gas gap actuator, the interaction of three absorbing compressor elements and of the low pressure stabilizing bed, the differences between the various compressor elements, check valves hysteresis, cold end intrinsic fluctuations etc. But among these, only few have a quantitatively relevant impact on the cooler performance.

The major contributions to the fluctuations are given by the **non-linear behavior of the hydride** (of the order of 40 mK) and by the **local temperature fluctuations of the radiator**, to which the compressor is mechanically and thermally anchored. The temperature oscillations of the absorbing compressor elements influence their pumping speed and consequently the pressure of absorption.

A compressor tuning operation is then needed to minimize a second source of fluctuations; those derived by the gas gap actuators timing. During normal cooling operation there are three compressor elements absorbing at the same time in each cycle phase. If the compressor element that is cooling reaches the absorption temperature too soon, there will be a short period of time in which there will be four compressor elements absorbing. Conversely, if the cooling phase is longer than the cycling time, there will be a period in which there are only two compressor elements absorbing. The possibility of having more (or less) than three compressor elements absorbing for more than few seconds introduces dramatic changes in the pumping speed characteristic of the compressor and therefore larger temperature fluctuations. The low-pressure bed

(that damps possible pressure fluctuations in the low-pressure line) can in fact only take care of short term instabilities during the transition of absorbing compressor elements. The time of cooling phase of each compressor element needs to be tuned by controlling the timing for turning on the gas gap actuator. The current design of the gas gap actuator allows a compressor cooling time of less than 450 seconds, which is less than the 667 currently chosen as the baseline cooler phase time.

Despite the fact that each compressor element is built according to exactly the same design and procedures, it is practically impossible to realize truly identical beds. A non-homogeneous behaviour can be noticed from bed to bed: this can result in pressure fluctuations inside the high-pressure line. In order to partially reduce this effect, a system of ballast tanks is present in the line. It is worthwhile to mention here another contribution to temperature instabilities: in the cold-end reservoirs and piping, the hydrogen collected is in a gas-liquid mixture status. From the interactions between these two phases, pressure, and so temperature, oscillations can arise. While in the piping it is possible to force the boiling of the extra liquid before it can go back up too much in the low-pressure line, in the reservoirs only an accurate design can minimize this effect. In the Planck sorption cooler we estimate this contribution to be at least an order of magnitude lower than the compressor fluctuations, but only accurate measurements will confirm this point.

Other intrinsic fluctuations present in the cold-end system, due to different physical processes, are expected to be practically negligible for our analysis and for this reason are not considered.

3.3 Simulation of temperature fluctuations at the Sorption Cooler Cold End

The thermal model of the Planck Sorption Cooler is realised using the SINDA software package. In our analysis, the cold-end has been modelled by neglecting the effect of the liquid thermal capacity and of the gas/liquid interactions (evaporation – condensation), which represents a worst case analysis. Both of the simplifying assumptions are intended to be overestimated and will be soon removed when a full cold head fluid-thermal model using FLUINT is incorporated.

The simulations have been performed according to three different scenarios which are indicative of increasing levels of non-ideality in the behaviour of the Sorption Cooler Compressors:

1. **Case of 6-equal homogeneous compressors**. In this case the simulation describes the temperature fluctuation at the SCCE caused by compressor pressure oscillations when the sorption cooler works with six equal and homogeneous compressors (most ideal case).
2. **Case of 5-equal homogeneous compressors + 1 non-homogeneous compressor**. In this case the simulation describes the temperature fluctuation at the SCCE caused by compressor pressure oscillations when the sorption cooler works with five equal and homogeneous compressors and one compressor with a non-homogeneous hydride distribution.
3. **Case of 3-equal homogeneous compressors + 3 non-homogeneous compressor**. In this case the simulation describes the temperature fluctuation at the SCCE caused by compressor pressure oscillations when the sorption cooler works with three equal and homogeneous compressors and three compressors with a non-homogeneous hydride distribution.

3.3.1 Case of 6-equal homogeneous compressors

Figure 3-2 shows the simulated temperature oscillation at the SCCE caused by pressure oscillations in an *ideally behaving* Sorption Cooler, with a compressor assembly composed by six equal beds with a homogeneous hydride distribution. From the figure it is apparent that the oscillation (with a peak-to-peak amplitude of about 40 mK) is *almost* sinusoidal, with a main frequency characterised by the compressor switch time (667s).

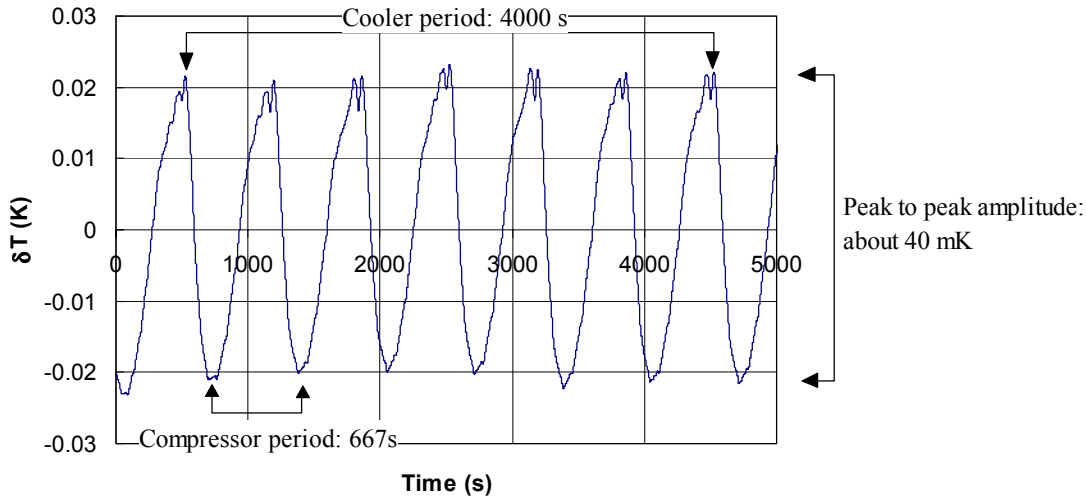

Figure 3-2. Simulation of temperature fluctuation at the SCCE for an ideally-behaving Sorption Cooler (6 equal compressors with homogeneous beds). The figure highlights the peak-to-peak amplitude of the temperature oscillation (40 mK), the cooler and the compressor periods (4000s and 667s respectively).

In Figure 3-3 we show the harmonic content of the oscillation in Fourier space. Note that in the abscissa axis we indicate the period rather than the frequency of the fluctuation and that the height of each peak represents the semi peak-to-peak amplitude of each harmonic. From the figure it is clear that although in this ideal case the oscillation is dominated by the switch time, there is a *tail* of high harmonics that is expanded in the inset. The main spin synchronous harmonics, in particular, are at the level of 0.6 mK (peak-to-peak) for the 60s component and of 0.1 mK (peak-to-peak) for the 30s component.

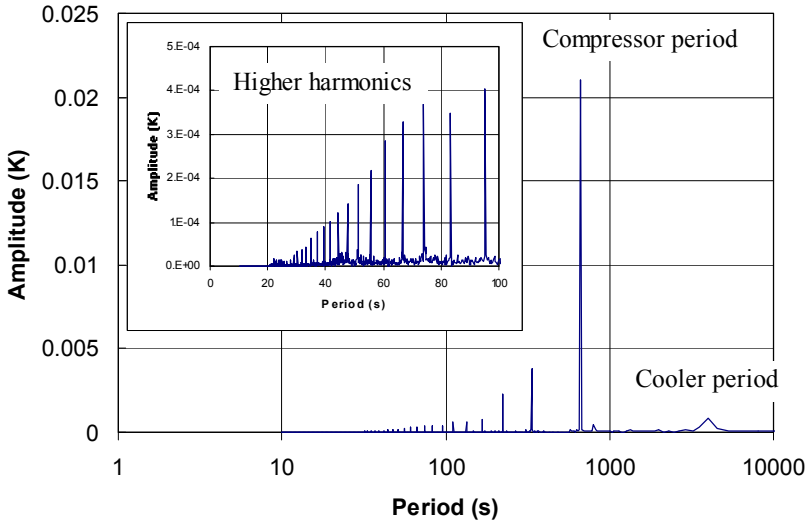

Figure 3-3. Fourier transform (amplitude vs. period) of the temperature oscillation in Figure 3-2. The figure shows that the main wave is the 667s compressor period. The inset figure is a zoom of the high frequency tail of the spectrum that shows that the main spin-synchronous components (60s and 30s) have amplitudes of 0.6 mK (peak-to-peak) and 0.1 mK (peak-to-peak), respectively.

3.3.2 Case of 5-equal homogeneous compressors + 1 non-homogeneous compressor

Figure 3-4 displays the simulated SCCE temperature oscillation curve for a Sorption Cooler composed by five equal and homogeneous beds plus one bed presenting non-homogeneities in the hydride distribution. The figure shows the dramatic qualitative change of the temperature oscillation shape introduced by the presence of one non-homogeneous sorption bed, in particular:

- the peak-to-peak amplitude of the fluctuation increases from 40 to 60 mK;
- the oscillation on the 4000s timescale (the cooler period) is more relevant;
- there is a higher content of high frequency components

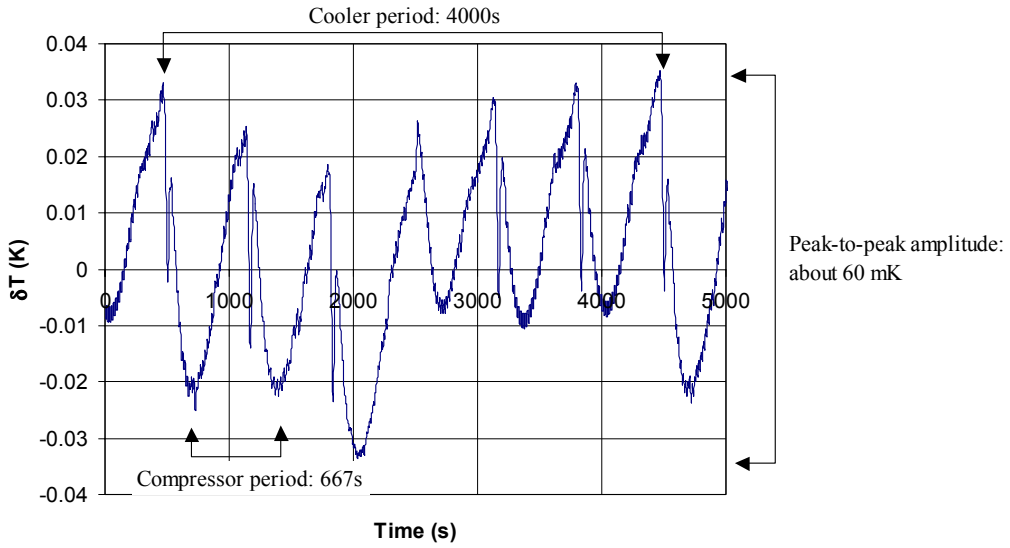

Figure 3-4. Simulation of temperature fluctuation at the SCCE for a Sorption Cooler characterised by 5 equal compressors with homogeneous beds and 1 compressor with non-homogeneous hydride distribution. The figure highlights the peak-to-peak amplitude of the temperature oscillation (about 60 mK), the cooler and the compressor periods (4000s and 667s respectively).

This is better clarified in Figure 3-5 that shows the signal in Fourier space. From the inset, in particular, we see that the 60s and 30s spin-synchronous components are at a level of approximately 2.5 mK (peak-to-peak) and 0.4 mK (peak-to-peak), respectively.

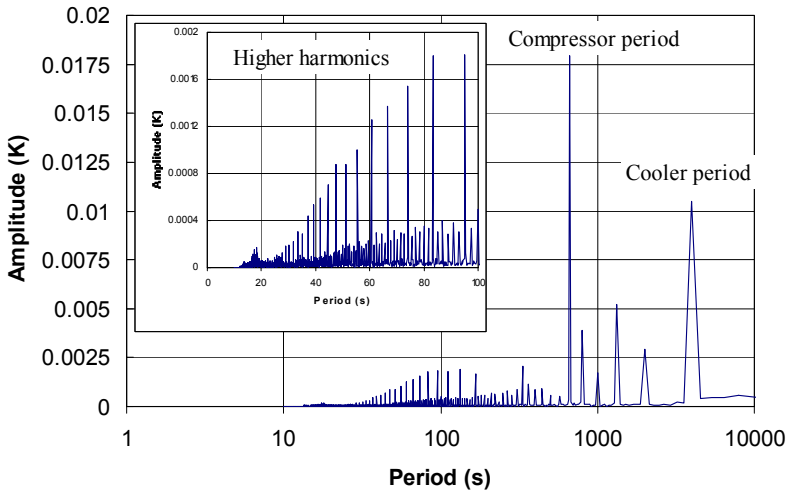

Figure 3-5. Fourier transform (amplitude vs. period) of the temperature oscillation in Figure 3-4. The figure shows that the presence of a non-homogeneous compressor bed determines an increase in the 4000s component (at the level of about 20 mK peak-to-peak) and of the high frequency tail, with the main spin-synchronous components (60s and 30s period) at the level of about 2.5 mK peak-to-peak and 0.4 mK peak-to-peak, respectively.

3.3.3 Case of 3-equal homogeneous compressors + 3 non-homogeneous compressors

The third scenario considered in this note is the one where the Sorption Cooler is characterised by three equal and homogeneous sorption beds and three beds with non-homogeneous hydride distribution. The curve (shown in Figure 3-6) is qualitatively similar to the one shown in Figure 3-4; in particular from the harmonic analysis (see Figure 3-7) we observe an increase in the total peak-to-peak amplitude and in the amplitude of the 4000s harmonic. Higher harmonics are still present but with a slightly smaller amplitude (1.7 mK and 0.4 mK peak-to-peak for the 60s and 30s components, respectively).

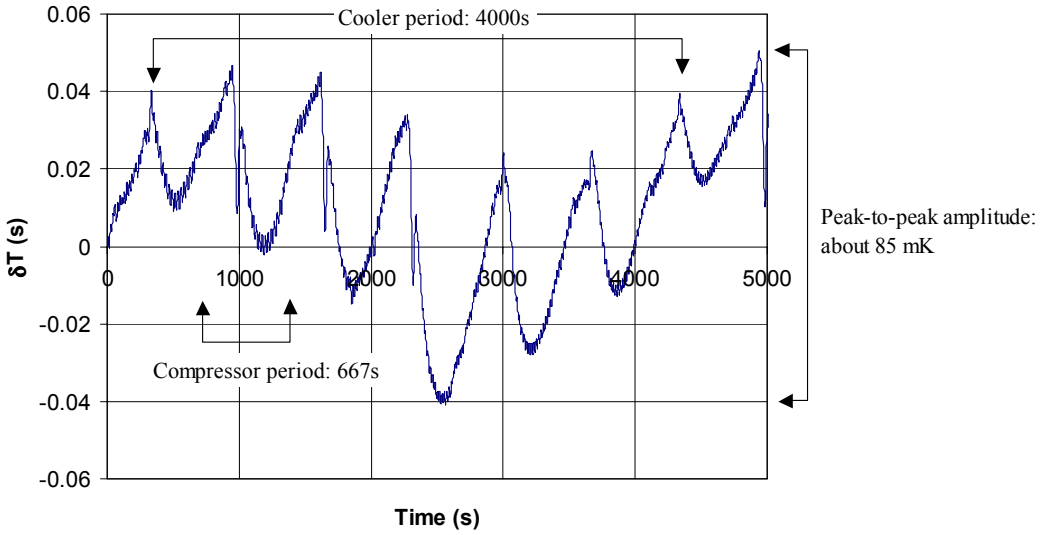

Figure 3-6. Simulation of temperature fluctuation at the SCCE for a Sorption Cooler characterised by 3 equal compressors with homogeneous beds and 3 compressors with non-homogeneous hydride distribution. The

figure highlights the peak-to-peak amplitude of the temperature oscillation (about 80 mK), the cooler and the compressor periods (4000s and 667s respectively).

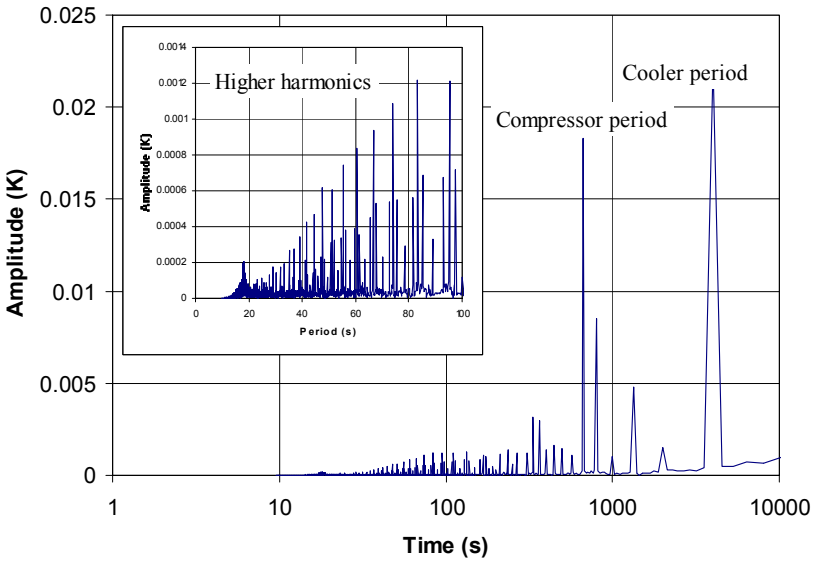

Figure 3-7. Fourier transform (amplitude vs. period) of the temperature oscillation in Figure 3-6. The figure shows that an increase in the non-ideal behaviour of the compressor assembly increases the "long" frequencies; in this example the 4000s component is actually the dominant signal with a peak-to-peak amplitude of about 40 mK. The high frequency tail is relatively unchanged with respect to the case shown in Figure 3-5.

4 Transfer of temperature oscillations from SCCE to LFI radiometers

In this section we discuss the propagation of thermal fluctuations from the Sorption Cooler cold end through the mechanical structure of the Low Frequency Instrument. In this study we have used the LFI thermal model to derive the damping factor of thermal oscillations of different periods for the four frequency channels.

4.1 LFI thermal model

In this section we provide a brief description of the LFI thermal model used in this study. Simulations have been made with the software ESARAD for radiative aspects and ESATAN for conductive aspects. More details can be found in [2].

The model includes the following parts:

- boundaries,
- Main Frame (MF),
- Feed Horns and FEMs,
- Waveguides (WGs),

- Harness

The following view shows a general picture of the LFI geometrical model realised with ESARAD: this is the model used for the simulations with Planck ALCATEL thermal model.

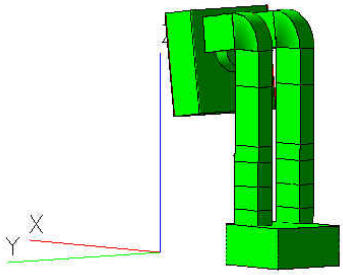

Figure 4-1.LFI radiative-geometrical thermal model

Each part that composes the LFI has been modelled in detail in order to obtain results most precise and elaborate. In the following paragraphs the various parts that compose the LFI thermal model will be briefly discussed.

4.1.1 Boundaries

The table lists the boundary nodes considered in this study. The temperatures have been obtained from the ALCATEL Plank thermal model.

Table 4-1 Boundary conditions

Node	Label	T (K)	Properties
122	MF SCC 20K	20	Area where the LR2 is fixed on
150	HFI Top	4	ε = 0.4 (cavity effect of HFI horns)
161 198	HFI	4	ε = 0.05 (ext. HFI surface)
200 230	4K Load	4	ε = 0.95
250	HFI 18K	20	ε = 0.05 , plate where the 18K Cold Unit is fixed
5000	COND. ENV.	50.0*	Mech. I/F where the bipods are fixed
6000	WG S3	50.0*	Zones where the WGs are linked to the 3rd shield
65500	RAD. ENV.	35**	ε = 1 , FPU black body radiative environment.

* : value from the analysis at ALCATEL telescope level
**: black body temperature which gives to FPU 10 mW as radiative heat flux. Value calculated by the results obtained with the telescope model.

At this step of the study the thermal model of the BEU is not available, but the BEU contribution has been simulate as boundary.

4.1.2 Main Frame

The MF is composed by 71 nodes (included the 122 boundary node). Many of these nodes are used to model the MF cold plate where is fixed the LR2 Cold Unit, a critical area for the calculation of MF distribution temperature and FEM stability.

The MF material is Al6061 and the surface emissivity ε is 0.05.

The thermal stability analyses have been performed using the MF detailed model shown in the picture below (radiative model).

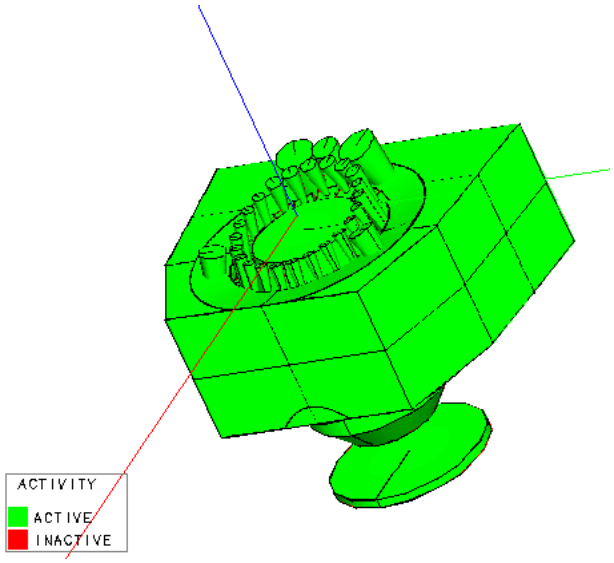

Fig. 4-2 LFI-FPU radiative thermal model

4.1.3 Feed Horns and FEMs

The FEU nodes are considered of material AL6061 and Copper. Detailed model of single Horns will be developed. At this moment, simplify model is sufficient to evaluate the thermal uniformity and noise damping.

The figure below show the radiative model of all the Feed Horns and FEMs

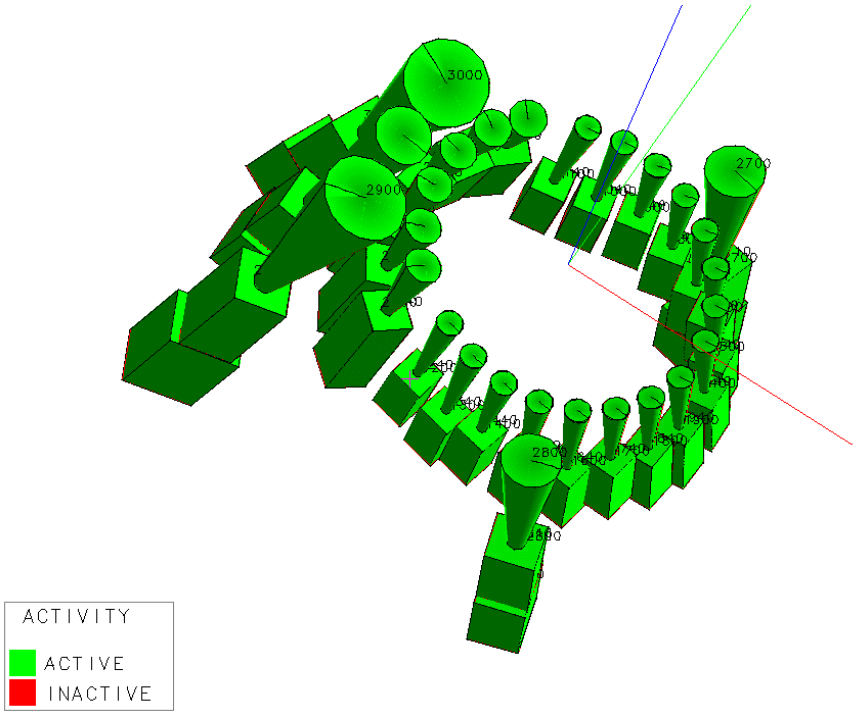

Fig. 4-3 FPU radiative thermal model

4.1.4 Waveguides (WGs)

Our conductive model is designed considering thermal resistances from all the WGs, while the radiative aspects are modelled considering two big bundles instead of the detailed representation of all the 108 waveguides. The figures below show both conductive and radiative models.

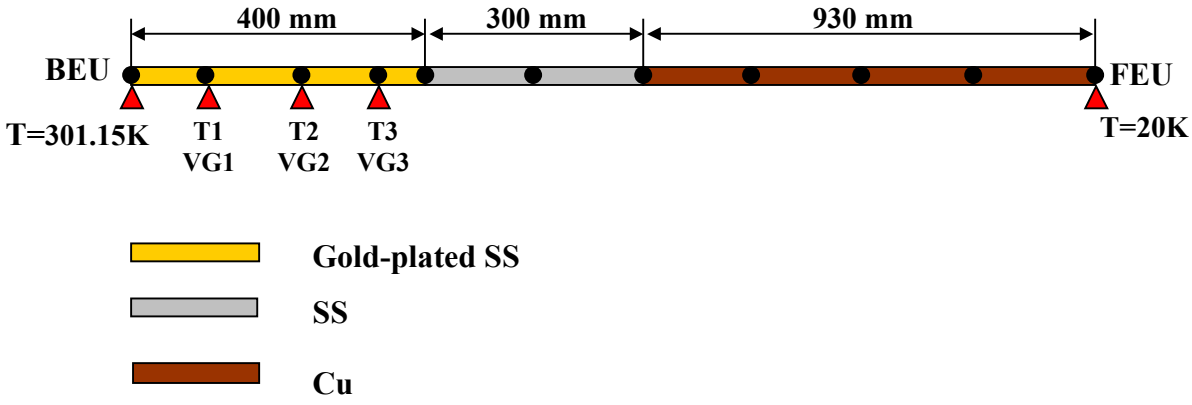

FIG. 4-4 Conductive thermal model of LFI waveguides

The thickness values of the various parts of the WGs are:

- SS: thickness = 0.254 mm
- AU: thickness = 2 μm
- CU: thickness = 0.4 mm

The nominal distances (provided by ALCATEL) between the various V-grooves (VGs) are:

- Distance BEU→VG1 = 79 mm
- Distance VG1→VG2 = 118 mm
- Distance VG2→VG3 = 122 mm

The materials considered for the various parts of the WGs are: SS, AU, CU.

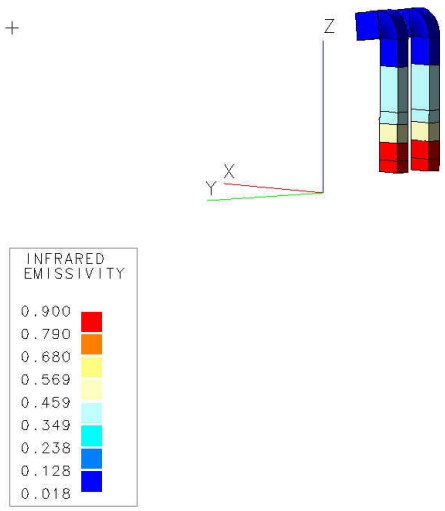

FIG. 4-5 Emissivity of LFI waveguides

4.1.5 Harness

We are analysing different material designs in order to optimise the FPU heat loads. Preliminary calculations were performed with the cable materials reported below.

Table 4-2: List of materials compatible with the manufacturing of the cryo-harness.

Materials for wires	Diameter
Aluminium (Al)	30 AWG … 40 AWG
Gold (Au)	30 AWG … 40 AWG
Phosphor-Bronze	30 AWG … 40 AWG
Copper (Cu)	30 AWG … 40 AWG
Nickel (Ni)	30 AWG … 40 AWG
Platinum (Pt)	30 AWG … 40 AWG
Titanium (Ti)	30 AWG … 40 AWG
Constantan	30 AWG … 40 AWG
Manganin	30 AWG … 40 AWG

In Table 4-3 we sum up a preliminary configuration of the cables in LFI harness

Table 4-3: Configuration of cables in LFI harness

FEM I/F		20-60K	60-300K
Wire	**Number of wires**	**Material AWG**	**Material AWG**
HEMT Drain	108	Ni – 38	Al - 40
HEMT Gate	216	Mang – 40	Mang - 40
Pswitch	216	Ti – 40	Bronze(P) - 38
Common GND Pswitch	27	Ti – 34	Bronze(P) - 38
Common GND HEMT	27	Ni – 38	Al – 34
	594		
Shield		Al	Al
Temperature sensors	48	Mang - 40	Mang – 40
GRAND TOTAL	**642**		

The final design is TBC.

4.2 Damping of thermal fluctuations by LFI thermal mass

In Figure 4-6 we show curves representing the damping factor of thermal fluctuations at the SCCE by the LFI mechanical structure as a function of the period of the temperature oscillation. Before applying these values to our analysis it is worth underlying the following issues:

- the plotted damping factors refer to the expected damping at the level of the front-end modules. In general the damping factor at the OMT and feed-horn levels will be greater than what is shown in the figure (thanks to the extra mass); on the other hand a reliable calculation of these factors is strongly dependent on a detailed implementation of the geometry of the feed-OMT system in the thermal model, which is currently not available. Therefore in the following of our analysis **we will conservatively consider the values displayed in Figure 4-6 as representative of the expected damping factor at the whole front-end radiometer (feed-OMT + FEM)**;

- the LFI mechanical structure will, in general, induce also a phase shift in the temperature oscillation between the SCCE and the front-end modules. A *relative* shift in the oscillation phase *between radiometers in the same frequency channel* could actually help to reduce the effect when combining data from different radiometers; our thermal simulations, however, have shown that the maximum *relative* phase shift (between radiometers belonging to different frequencies) is quite small, i.e. less than 10%. Therefore we adopt a **conservative criterion assuming no relative change in the temperature fluctuation between radiometers in the same frequency channel**;
- the damping factors shown in Figure 4-6 are relative to one particular FEM for each frequency (in particular we have chosen the following: LFI28 at 30 GHz, LFI24 at 44 GHz, LFI21 at 70 GHz and LFI10 at 100 GHz. In general these curves will be different for each FEM, because of the different position with respect to the SCCE. Considering that the LFI mechanical structure is still to be frozen, we have preferred to maintain the study at a simpler level and wait for a more definitive mechanical layout for a more detailed analysis of the thermal damping.

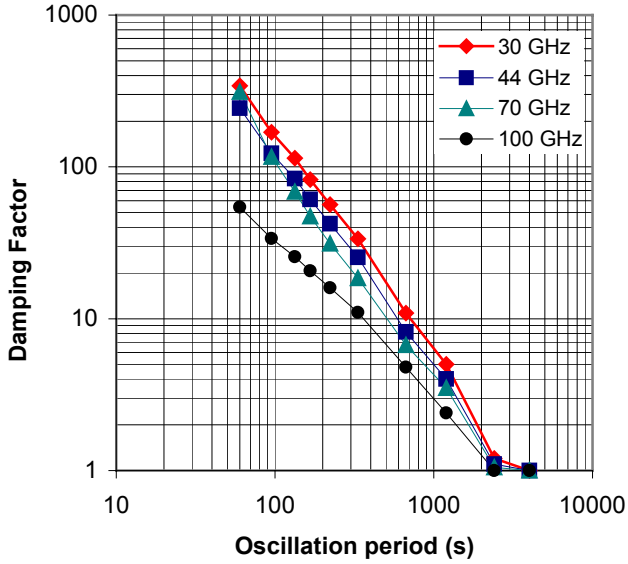

Figure 4-6. Damping factor of thermal fluctuations as a function of the period of different harmonics for the four frequency channels. The graph shows that the LFI mechanical structure is a "low-pass" filter for thermal fluctuations. In general the damping factor is higher for the low frequency radiometers which have a higher (thermal) mass.

The above figure shows clearly that the LFI structure is basically a *low-pass* filter for thermal fluctuations. The damping factor is generally dependent both on the position and on the mass of the front-end modules; in fact the temperature instability will be highest for the 100 GHz FEMs (which are the smallest) and lowest for the 30 GHz FEMs (which are the largest).

The most dangerous spin-synchronous components will be reduced by a factor ranging from 50 to 300 while we expect a reduction of about 10 for the fluctuations synchronous with the switch time of 667s. The longest "waves" (like the 4000s signal of the whole cooler assembly) will be transmitted unaltered in amplitude from the SCCE to the instrument front-end. In Table 4-4 we list in detail the expected peak-to-peak amplitude of the main spin-synchronous component (60s) of the temperature fluctuation at the FEM level for he three Sorption Cooler scenarios considered in this note.

Table 4-4 – Peak-to-peak amplitude of the 60s (spin-synchronous) component of the temperature fluctuation at the FEM level. For a complete view of the spectral components see Fourier transforms in section 9.

Temperature fluctuation shape at SCCE	Peak-to-peak amplitude of 60s component of FEM temperature fluctuation (μK)			
	30 GHz	**44 GHz**	**70 GHz**	**100 GHz**
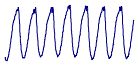	2.0	2.4	2.0	10.0
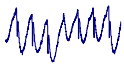	8.0	10.0	8.0	50.0
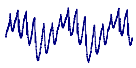	5.0	7.0	6.0	30.0

5 Sensitivity of radiometer measured signal from physical temperature fluctuations

The instrument transfer function (that converts the front-end physical temperature fluctuation into the corresponding error on the sky signal measurement) has been derived by making some simplifying assumptions concerning the different couplings of the front-end radiometers with physical temperature:

Feed+OMT and reference load antenna noise. This is a very important coupling, because at this level the fluctuations depend on the asymmetry of the radiometer chain. In theory it is possible to balance the asymmetry by choosing an appropriate value for the reference load insertion loss, in practice the objective will be to build reference load antennas with an insertion loss as similar as possible to the feed+OMT insertion loss.

Gain and noise temperature. Ideally a perfectly balanced radiometer (i.e. with equal sky and reference load signals and exactly null power output) would be insensitive both to gain and noise temperature fluctuations; although LFI approaches this ideal behaviour it has nevertheless some sensitivity to amplifier instabilities which can be induced also by oscillations in the physical temperature.

Reference load. The reference load signal can be affected by thermal effects essentially in two ways: (i) coupling with the reference load antenna and (ii) oscillations in the reference load signal induced by thermal couplings between LFI and HFI. The first coupling actually reduces the overall effect, because it increases the symmetry upstream the first hybrid; the second effect is quite more complicated to study because it is necessary to model in detail the radiative coupling between LFI and HFI. In our calculation we have considered only the first coupling (with the reference horn).

Insertion losses. In general the insertion losses of the various radiometer components (feed, OMT, hybrids, phase switches) depend on the physical temperature, but this dependence is weak for temperature changes of the order of 10 – 20 mK, and can therefore safely be neglected.

To calculate the induced signal fluctuation let us write the physical temperature as $T_{phys}(t) = T^0_{phys} + \delta T_{phys}(t)$ where $T^0_{phys} = 20\,\mathrm{K}$ and $\delta T_{phys}(t)$ is the oscillation. The change in the observed

signal, δT_s can be calculated analytically by solving the equation $\frac{\partial p}{\partial T_s}\delta T_s = \frac{\partial p}{\partial T_{phys}}\delta T_{phys}$ (where p is the radiometer power output) which leads to $\delta T_s = T_f \times \delta T_{phys}$, where T_f represents the transfer function given by:

$$T_f = L_{\text{feed-OMT}}\left\{\left(1-\frac{1}{L_{\text{feed-OMT}}}\right) - r\left(1-\frac{1}{L_{4K}}\right) + \left[\tilde{T}_s + T_n - r\left(\tilde{T}_{4K} + T_n\right)\right]\frac{\ln(10)}{10}\frac{\partial G_{\text{dB}}}{\partial T_{phys}} + (1-r)\frac{\partial T_n}{\partial T_{phys}}\right\}$$

Term arising from temperature fluctuations at Feed - OMT level

Term arising from temperature fluctuations at reference horn level

Dependence of gain on physical temperature

Dependence of noise temperature on physical temperature

(5-1)

In equation **(5-1)** $\tilde{T}_s(t)$ represents the sky signal *after the feed-OMT system*, equal to $\tilde{T}_s = \frac{T_s}{L_{\text{feed-OMT}}} + \left(1-\frac{1}{L_{\text{feed-OMT}}}\right)T_{\text{phys}}$, and $\tilde{T}_{4K}(t)$ represents the sky signal *after the reference load horn*, equal to $\tilde{T}_{4K} = \frac{T_{4K}}{L_{4K\text{ horn}}} + \left(1-\frac{1}{L_{4K\text{ horn}}}\right)T_{\text{phys}}$.

In the equation above the different terms relative to the various dependencies on the physical temperature can be easily recognised. In particular we see that the transfer function depends on level of signal unbalance at the level of the first hybrid input (i.e. $\delta = \tilde{T}_s - \tilde{T}_{4K}$), on the thermal stability of front end gain (term $\frac{\partial G_{\text{dB}}}{\partial T_{phys}}$) and noise temperature (term $T_n' = \frac{\partial T_n}{\partial T_{phys}}$) and on the gain modulation factor, r; in particular:

- the signal unbalance δ will not be know with a high precision but it is not expected to vary in flight as it is determined mainly by the insertion losses of the Feed-OMT system and of the 4K reference horn. Considering reference load signal of the order of 5K and front-end passive components with insertion losses in the range 0.2dB – 0.3dB we can expect δ to be fixed at a value in the range **-1.4K to -2.3K**;
- cryogenic measurements performed on LNA's at low frequency (2 to 8 GHz) show that T_n' range from 0.15 to 0.3 K/K; considering the much higher frequency of LFI radiometers we will consider a value of **0.8 K/K** for T_n';
- gain sensitivity to physical temperature oscillations is generally very small; room temperature measurements performed on 20dB LNA's have shown gain variations of the order of **-0.05 dB/K**, which are probably much lower at cryogenic temperatures;
- the gain modulation factor will be determined from raw sky and load data (TBC) and will be fixed to a value in order to give the best balance of the whole radiometer chain ($r \approx (T_{sky} + T_{sys}) / (T_{load} + T_{sys})$). This value is expected to be known with a **precision of the order 10^{-3}** [4] and will be updated during flight every TBD days.

Considering the above estimates for the relevant parameters in equation **(5-1)** we can fix values for the transfer function at the different frequencies:

Table 5-1 – Values of the radiometer transfer function for front-end thermal fluctuations. In the table are also reported the parameters used in equation (5-1)

	30 GHz	**44 GHz**	**70 GHz**	**100 GHz**
$L_{feed-OMT}$ **(dB)**	0.25	0.25	0.25	0.3
L_{4K} **(dB)**	0.2	0.2	0.2	0.2
T_{4K} **(therm. temp, K)**	5.5	5.5	5.5	5.5
T_{phys} **(K)**	25	25	25	25
T_n **(K)**	8.6	14.1	25.7	46.7
$\partial G_{dB} / \partial T_{phys}$ **(dB/K)**	-0.05	-0.05	-0.05	-0.05
$\partial T_n / \partial T_{phys}$ **(K/K)**	0.8	0.8	0.8	0.8
r	0.82350	0.87210	0.92140	0.95671
T_f	**0.16916**	**0.12590**	**0.08197**	**0.05965**

From the values in Table 5-1 it is apparent that the higher frequency radiometers are less sensitive to front-end physical temperature fluctuations. This can be understood considering that in equation **(5-1)** the main contribution comes from the noise temperature term (i.e. the term $(1-r)\times \partial T_n / \partial T_{phys}$) that is smaller at higher frequencies, where the gain modulation factor is closer to 1.

In the following table we list the peak-to-peak amplitude of the 60s component of the signal oscillation induced by front-end temperature oscillations (values have been obtained by multiplying the amplitudes in Table 4-4 by the transfer function values in Table 5-1). These values are of particular relevance because they represent the expected spin-synchronous systematic error expected on the final maps, which cannot be further reduced by the scan strategy and by post-processing the data with destriping algorithms.

Table 5-2 – Peak-to-peak amplitude of the 60s (spin-synchronous) component of the induced signal fluctuation. Values are given in both antenna and thermodynamic temperatures (latter are shown in brackets).

Temperature fluctuation shape at SCCE	Peak-to-peak amplitude of 60s component of induced signal fluctuation (μK)			
	30 GHz	**44 GHz**	**70 GHz**	**100 GHz**
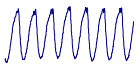	0.34 (*0.35*)	0.30 (*0.31*)	0.16 (*0.18*)	0.60 (*0.77*)
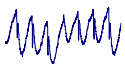	1.35 (*1.38*)	1.26 (*1.32*)	0.66 (*0.75*)	2.98 (*3.83*)
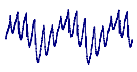	0.85 (*0.87*)	0.88 (*0.92*)	0.49 (*0.55*)	1.79 (*2.30*)

6 Systematic error in final LFI maps

6.1 Maps before destriping

In this section we present results describing the expected systematic error in the final LFI maps. The maps shown here contain only the spurious signal induced by thermal fluctuations of the frond-end without any sky signal or instrument noise superimposed. They have been produced using the HEALPix pixellisation scheme with the values of the n_{side} parameter indicated in Table 6-1.

Table 6-1 – HEALPix pixellisations used in this study.

	30 GHz	44 GHz	70 GHz	100 GHz
N_{side}	256	256	512	1024
pixel size (arcmin)	13.7	13.7	6.85	3.4

The obtained maps are summarised in Figures 6-1 through 6-4; **each one is relative to a single channel**, i.e.: LFI27 (30GHz), LFI25 (44GHz), LFI20 (70 GHz) and LFI09 (100 GHz). It is worth noting that the final frequency maps will be obtained by co-adding all the maps in each frequency channel, which in principle provides an additional damping factor of the systematic effect. This additional damping is negligible at low frequencies while it is expected to be of the order of 2 – 2.5 for the 70 and 100 GHz channels.

30 GHz – LFI27

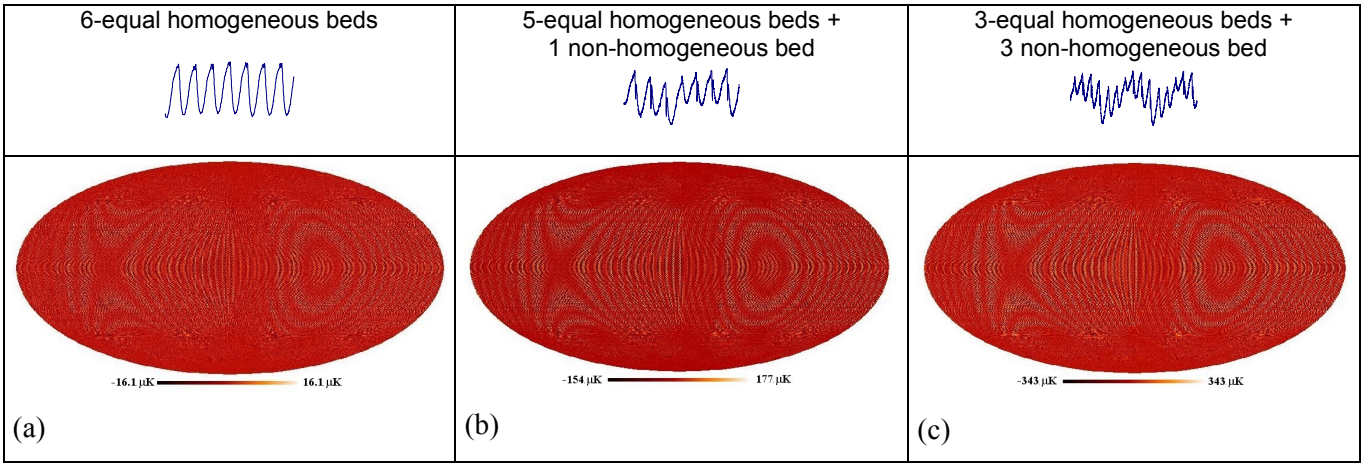

Figure 6-1. Map of the final systematic error (antenna temperatures) relative to the 30 GHz LFI27 channel for the three Sorption Cooler scenarios considered in this note.

44 GHz – LFI25

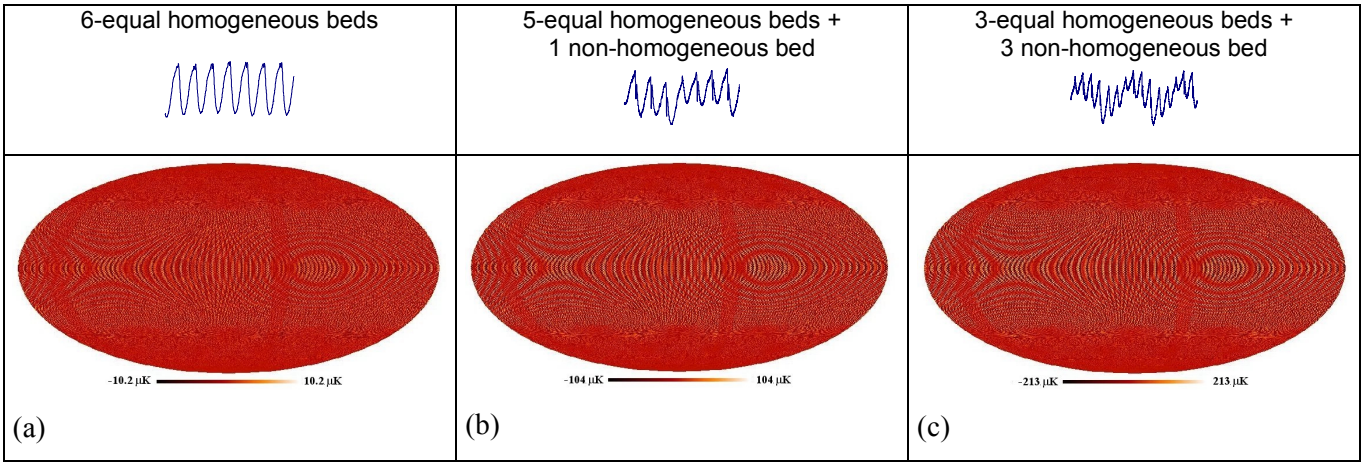

Figure 6-2. Same as in Figure 6-1 for the 44 GHz LFI25 channel.

70 GHz – LFI20

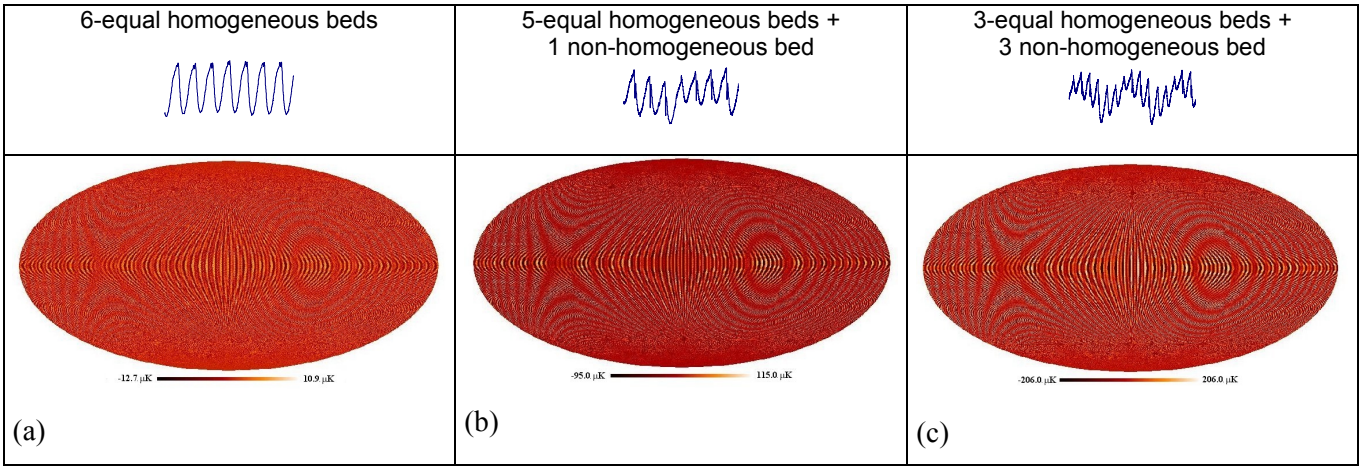

Figure 6-3. Same as in Figure 6-1 for the 70 GHz LFI20 channel

100 GHz – LFI09

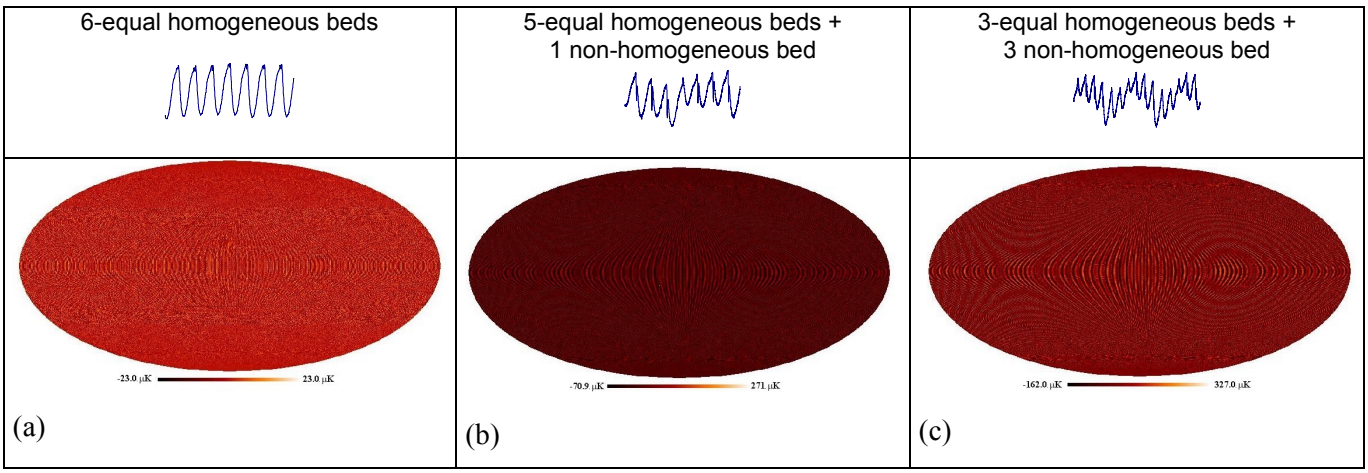

Figure 6-4. Same as in Figure 6-1 for the 100 GHz LFI09 channel.

The peak-to-peak amplitude of the systematic effect is dependent on the choice of the map pixel size, which is approximately 1/3 of the FWHM (see values reported in Table 6-1). Because the requirements on the maximum acceptable systematic error have been set on a pixel of a size equal to the FWHM, it is necessary to rescale the values from the maps to a larger pixel. In principle this can be done by analysing the map power spectra, which contain all the relevant statistical information at angular scales larger than the map pixel size.

In our case we have preferred to adopt a less rigorous approach, which is in turn much simpler and faster. Each map has been "degraded" (which means projected with a greater pixel size) to values of the parameter N_{side} as low as 32 (which corresponds to a pixel size of about 109') and the peak to peak amplitude of the systematic effect has been plotted against the map pixel size. Figure 6-5 shows such behaviour relatively to the case represented in Figure 6-4(c); the plot clearly shows that the amplitude of the systematic error does not scale linearly with the pixel size but it decreases much faster. A more exhaustive analysis in terms of the impact on the angular power spectrum recovery are in progress. In the figure we also show a best fit with a 3rd order polynomial of the type $a_n x^{-n}$.

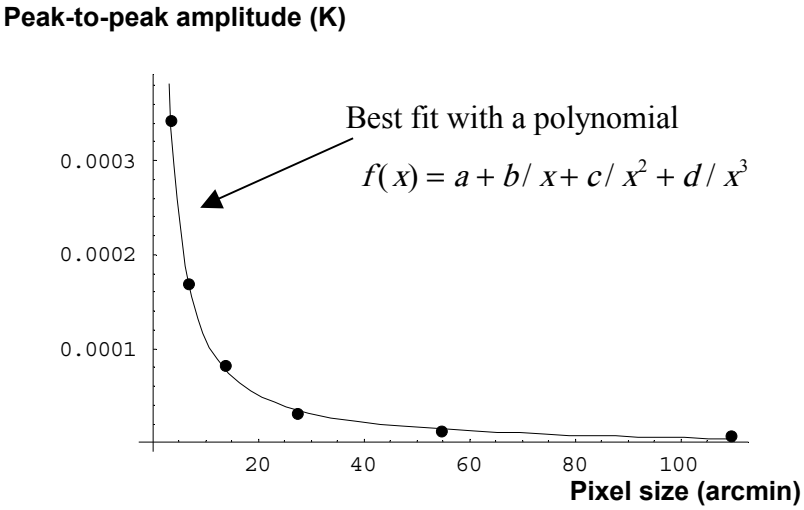

Figure 6-5. Example showing the behaviour of the peak-to-peak amplitude of the systematic effect on the map versus the pixel size. The figure shows that the decrease with pixel size is not linear but it is best fitted with a 3rd order polynomial of the type $a_n x^{-n}$

In Table 6-2 we report a summary of the expected maximum systematic error on the LFI maps before applying destriping algorithms. The values are reported as thermodynamic temperatures and have been scaled to a pixel size equal to the beam FWHM. In the table we also split the total into spin synchronous (see Table 5-2) and non-spin synchronous components, assuming linear additivity. These results show that the expected effect is of several μK per pixel, even in the most favourable scenario. In particular the spin synchronous component (that cannot be reduced by data processing), is of the order of 1 – 2 μK peak-to-peak, which is higher that the maximum acceptable value budgeted in Table 2-1.

Table 6-2 – Summary of maximum systematic errors induced by front-end temperature fluctuations (before destriping). Values are relative to a pixel equal to the beam FWHM.

	Peak-to-peak amplitude of thermally-induced systematic errors final map (μK – thermodynamic temperature)											
Temperature fluctuation shape at SCCE	**30 GHz – LFI27**			**44 GHz – LFI25**			**70 GHz – LFI20**			**100 GHz – LFI09**		
	Beam size = 36′			*Beam size = 29′*			*Beam size = 17′*			*Beam size = 12′*		
	60s	*Other periodic*	***Total***	*60s*	*Other periodic*	***Total***	*60s*	*Other periodic*	***Total***	*60s*	*Other periodic*	***Total***
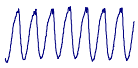	0.3	5.4	***5.7***	0.3	5.2	***5.5***	0.2	10.5	***10.7***	0.8	14.3	***15.1***
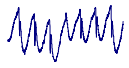	1.4	64.8	***66.2***	1.3	50.5	***51.8***	0.8	97.8	***98.6***	3.8	108.7	***112.5***
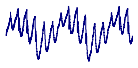	0.9	140.3	***141.2***	0.9	111.6	***112.5***	0.6	203.4	***204.0***	2.3	220.3	***222.6***

6.2 Estimation of additional damping from destriping

In this section we evaluate the residual systematic error on the maps after the application of a "destriping" code [5] developed by the LFI team for reducing the impact of $1/f$ noise fluctuations.

This code generally uses averaged one-hour scan circles (although it has the capability to work with all the single scan circles); because averaging acts like a low-pass filter then only the very low frequencies remain in the map as a residual effect. The basic hypothesis is that for each circle the residual effect can be well approximated as a constant additive level related to the mean level of the spurious fluctuation during the scan. The code optimises these levels by minimising the map temperature values in pixels observed by more than one scan circle during the mission. Further details of the code implementation can be found in [5].

Although this code has been implemented for removing correlated stripes from $1/f$ noise [6], it has been shown that it is capable of removing correlated effects from periodic fluctuations [7] even if they are embedded in white + $1/f$ noise. This means that the presence of noise in the data stream does not change the ability of the destriping code of removing these periodic effects.

In Figure 6-6 through Figure 6-9 we show the maps obtained after the application of the destriping code to the time ordered data obtained in the three Sorption Cooler scenarios for the four LFI frequencies.

30 GHz – LFI27

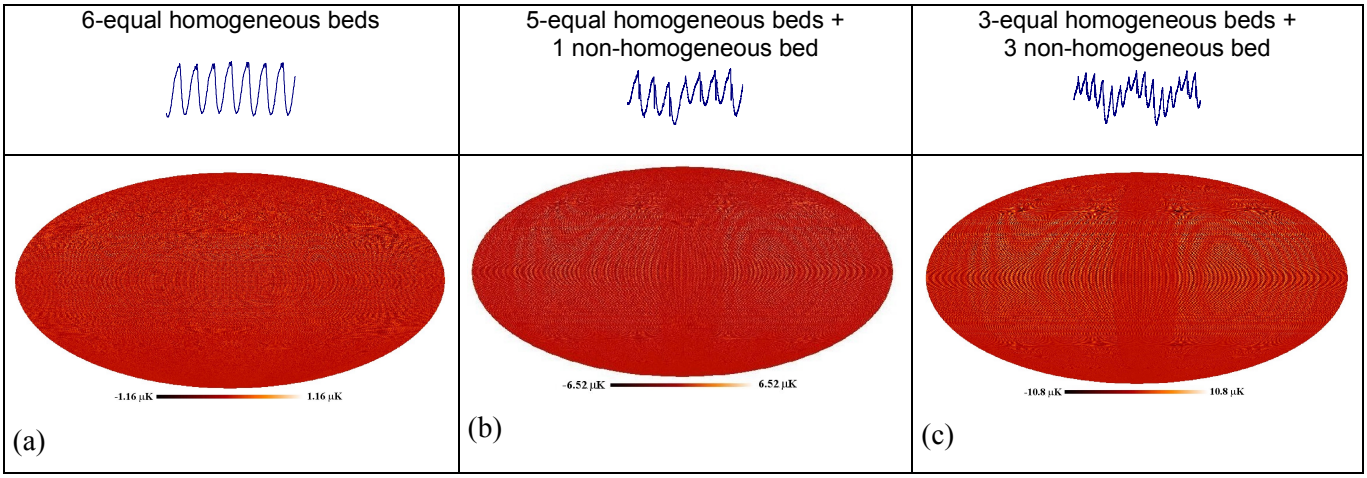

Figure 6-6. Map of the final systematic error after destriping (antenna temperatures) relative to the 30 GHz LFI27 channel for the three Sorption Cooler scenarios considered in this note.

44 GHz – LFI25

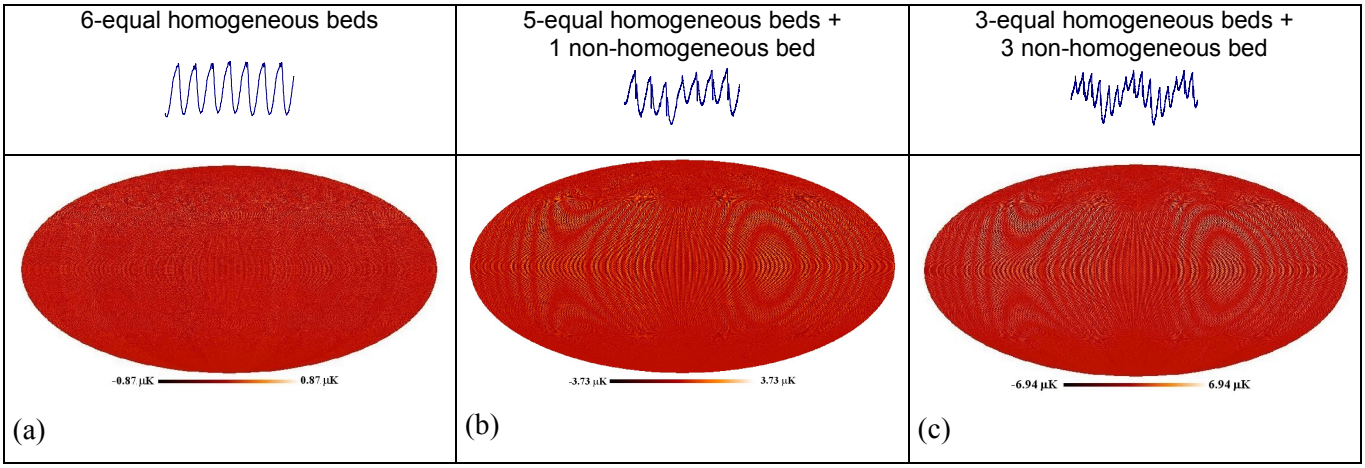

Figure 6-7. Same as in Figure 6-1 for the 44 GHz LFI25 channel.

70 GHz – LFI20

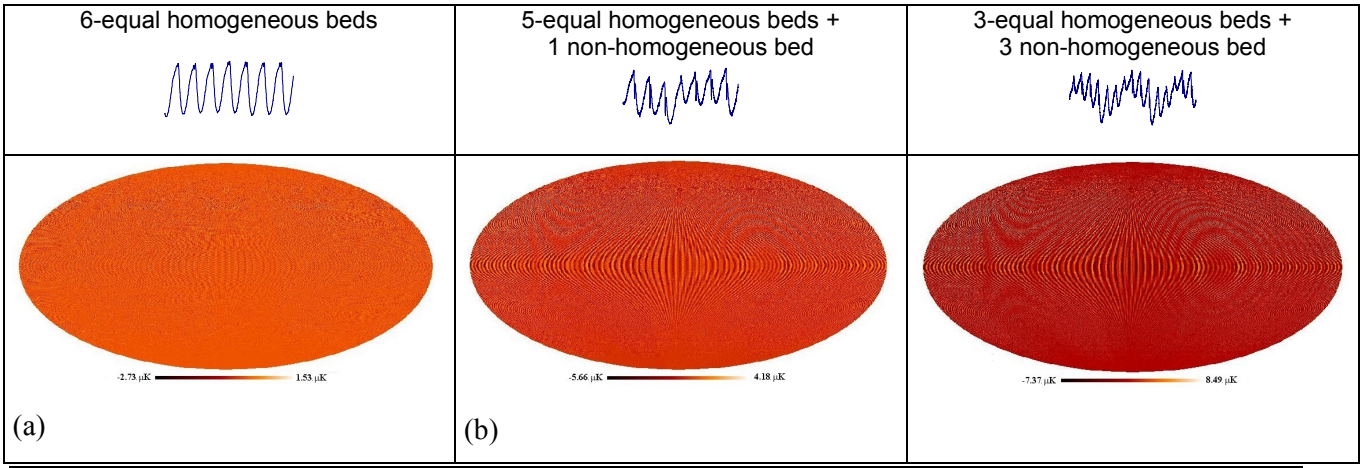

		(c)

Figure 6-8. Same as in Figure 6-1 for the 70 GHz LFI20 channel

100 GHz – LFI09

6-equal homogeneous beds	5-equal homogeneous beds + 1 non-homogeneous bed	3-equal homogeneous beds + 3 non-homogeneous bed
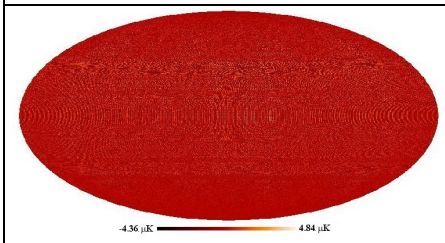	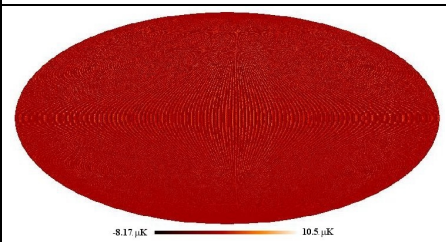	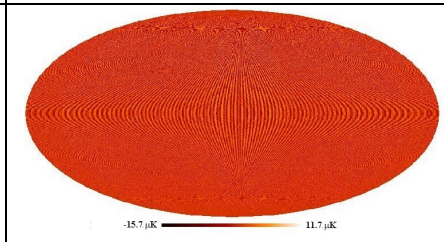
(a)	(b)	(c)

Figure 6-9. Same as in Figure 6-1 for the 100 GHz LFI09 channel.

The last step is to evaluate the residual peak-to-peak effect on a pixel size equal to the beam FWHM, in order to obtain estimates that can be compared with the requirements specified in Table 2-1. This has been performed according to the same procedure used in section 6.1 to obtain the values of Table 6-2.

Table 6-3 – Summary of maximum systematic errors induced by front-end temperature fluctuations (after destriping). Values are relative to a pixel equal to the beam FWHM. Different colours indicate values which are inside requirements (green), slightly out of requirements (orange) and well out of requirements (red).

	Peak-to-peak amplitude of thermally-induced systematic errors in final maps after destriping (μK – thermodynamic temperature)											
Temperature fluctuation shape at SCCE	**30 GHz – LFI27**			**44 GHz – LFI25**			**70 GHz – LFI20**			**100 GHz – LFI09**		
	Beam size = 36′			*Beam size = 29′*			*Beam size = 17′*			*Beam size = 12′*		
	60s	*Other periodic*	***Total***	*60s*	*Other periodic*	***Total***	*60s*	*Other periodic*	***Total***	*60s*	*Other periodic*	***Total***
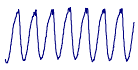	0.35	0.21	***0.56***	0.31	0.34	***0.65***	0.2	0.9	***1.1***	0.8	1.1	***1.9***
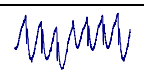	1.4	1.1	***2.5***	1.3	1.1	***2.4***	0.8	2.9	***3.7***	3.8	1.3	***5.1***
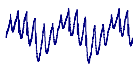	0.9	4.4	***5.3***	0.9	3.6	***4.5***	0.6	6.8	***7.4***	2.3	7.0	***9.3***

From the values reported in the above table it is possible to draw the following considerations:

1. the impact of thermal fluctuations increases with increasing non-ideality in the Sorption Cooler behaviour. This was clearly expected from the analysis discussed in section 3.3, considering that increasing non-idealities in the behaviour of the cooler compressors cause temperature fluctuations with a higher amplitude and a greater harmonic content;
2. the impact of thermal fluctuations is greater for the channels at higher frequency. To understand this result we must consider that it derives from a balance among three different factors, i.e.: (i) the damping of thermal fluctuations by the LFI mechanical structure, which is more effective for the low frequency channels (see Figure 4-6), (ii) the radiometer transfer function, which is more favourable for the high frequency channels (see Table 5-1), (iii) the projection of the effect into the observed sky, which is less favourable for the high frequency channels, which have a smaller pixel size;
3. the 100 GHz channel is particularly sensitive to spin-synchronous harmonics. This is an effect of the less effective damping of the mechanical structure (see Figure 4-6);
4. the final results indicate that if we assume that the Sorption Cooler will not behave ideally the final effect can be significant, of the order of several μK per pixel.

We must of course underline that the whole analysis is based on simulated scenarios for the cooler behaviour and that a more definitive answer will be available when this analysis will be re-run with the first experimental data that will be obtained on the Sorption Cooler EBB (currently foreseen by the end of 2001). Furthermore our analysis is based on some conservative assumptions; the most relevant are: (i) the shape of temperature fluctuations are considered to be the same at the levels of the feed-OMT system and of the FEMs and (ii) the co-adding of maps from the different horns for each frequency channel is neglected. In particular the second assumption can lead to an overestimate of the effect by a factor 2 – 2.5 for the 70 and 100 GHz channels.

Despite the existing uncertainties and conservative assumptions our results indicate that if the simulated scenarios will be confirmed by the experimental data then it will be necessary to improve the front-end thermal stability by at least one order of magnitude, as it was already pointed out by both instruments on the basis of previous analyses.

7 Conclusions

In this technical note we have analysed the impact of LFI front end temperature fluctuations on LFI measurements. In our simulations we have considered different stability scenarios of the Sorption Cooler cold end obtained by simulations of the behaviour of the compressor assembly. These simulations indicate that a non homogeneous hydride distribution in the compressors increases both the amplitude and the harmonic content of temperature oscillations.

The shape of these fluctuations is very much different at the level of the front-end modules. In fact the LFI structure acts like a low-pass filter, thus cutting the high frequency tail of these fluctuations by a factor of about 100. The lowest frequencies, instead (in particular the 4000 s period of the whole compressor assembly), is transmitted relatively unaltered. The thermo-mechanical filtering (which depends on the thermal mass and thermal resistance encountered by thermal oscillations) has been shown to be more effective for the low frequency channels (30 and 44 GHz).

Thermal instabilities impact on the radiometer performances because they induce a signal oscillation caused by the front-end passive components and by temperature-driven gain and noise temperature fluctuations. Although the current design of LFI radiometers aims at obtaining as much balance as possible between the

sky and the reference load signals, the instrument shows a non-negligible sensitivity to front end temperature instability. This sensitivity is higher for the low frequency channels which are characterised by a lower noise temperature. With the current expected front-end temperature fluctuations the signal at the radiometer output is expected to vary at the mK level peak-to-peak.

The damping of this effect determined by the measurement redundancy and by post-processing the data with destriping algorithms is such that the final peak-to-peak amplitude of the effect on final maps (pixel size equal to the FWHM) is in the range 0.5 – 9.0 μK. A comparison with the systematic error budget indicates that only in the case of an ideally behaved Sorption Cooler the expected effect is compliant with this budget. Although a more definitive picture will be available when the first experimental results on the Sorption Cooler EBB will be released, it is expected that an improvement of at least one order of magnitude in the front end temperature stability will be necessary.

8 References

[1] Mennella, A., and Bersanelli, M: "Effect of Sorption Cooler Temperature Variations on LFI Front-End", PL-LFI-PST-TN-005, June 2000.

[2] Ferretti, R., Pagan, L.: "Thermo Mechanical Study of the Main Frame", draft technical note, September 2001.

[3] Bersanelli, M., *et al*: "PLANCK-LFI Scientific Requirements", PL-LFI-PST-SP-011, January 2001.

[4] Mennella, A., and Bersanelli, M: "Impact of Back-End temperature fluctuations on LFI", PL-LFI-PST-TN-029, September 2001.

[5] Maino, D., Maris, M., Burigana, C., Stanghellini, G., and Maltoni, M.: "PLANCK-LFI destriping code user's guide", PL-LFI-OAT-MA-002, April 2000.

[6] Maino, D., Burigana, C., Maltoni, M,. et al., 1999, A&ASS, 140, 383.

[7] Mennella, A., Bersanelli, M, Maino, D., Burigana, C., Stanghellini, L., Morgante, G.: "PLANCK-LFI: systematic effects induced by periodic fluctuations", A&A (submitted), October 2001.

9 Appendix – Shape of temperature fluctuations at front-end radiometers

9.1 Case of 6-equal homogeneous compressors

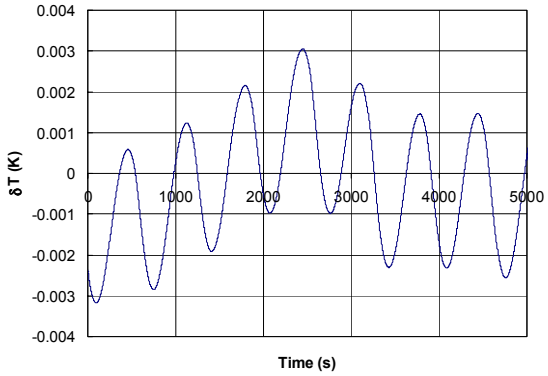

(a)

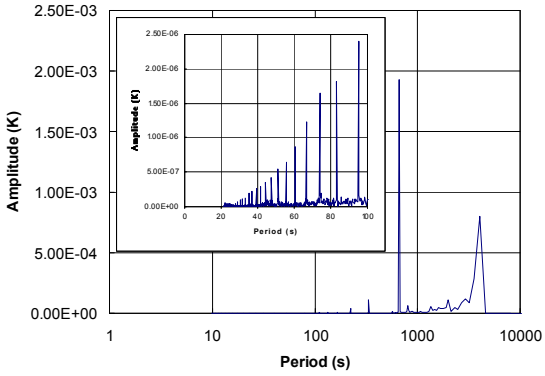

(b)

Figure 9-1. Expected temperature oscillation at the 30 GHz front-end radiometers considering an ideally behaving Sorption Cooler (6 equal compressors with homogeneous beds); (a) oscillation in time domain, (b) Fourier transform

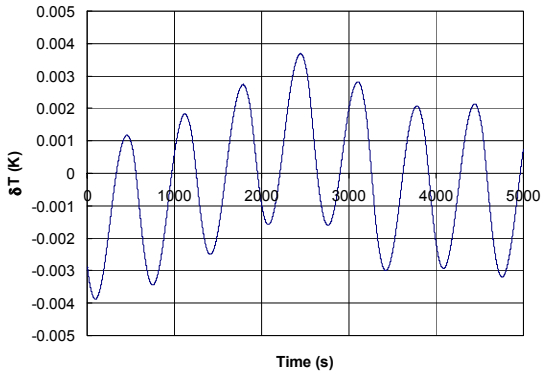

(a)

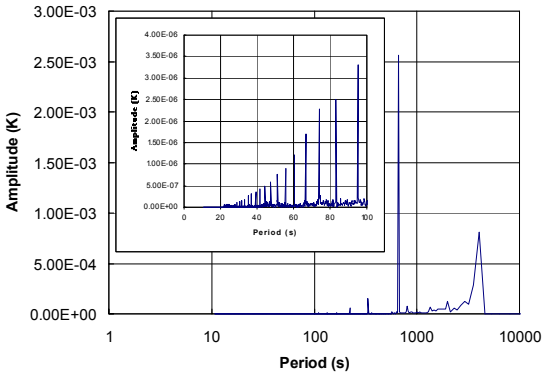

(b)

Figure 9-2. Same as in Figure 9-1 for the 44 GHz front-end radiometers.

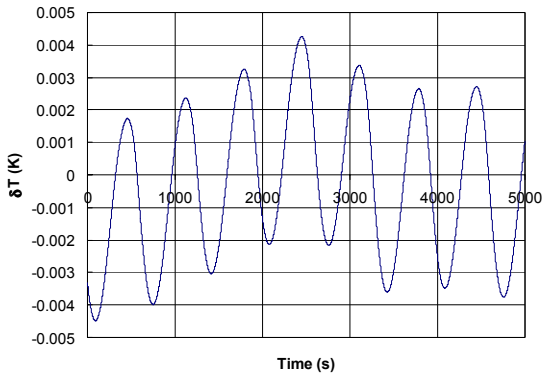

(a)

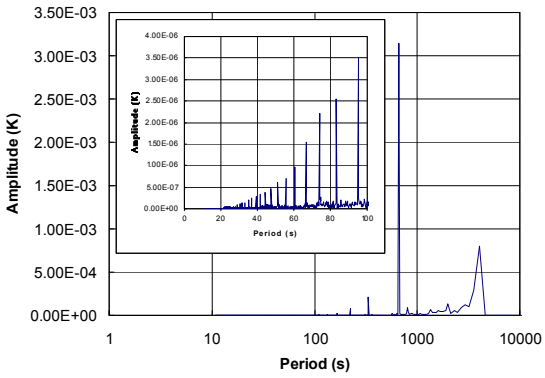

(b)

Figure 9-3. Same as in Figure 9-1 for the 70 GHz front-end radiometers.

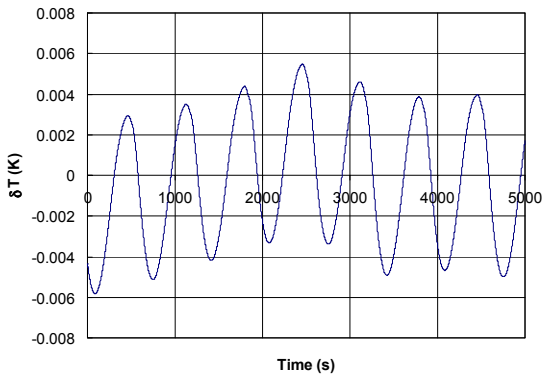

(a)

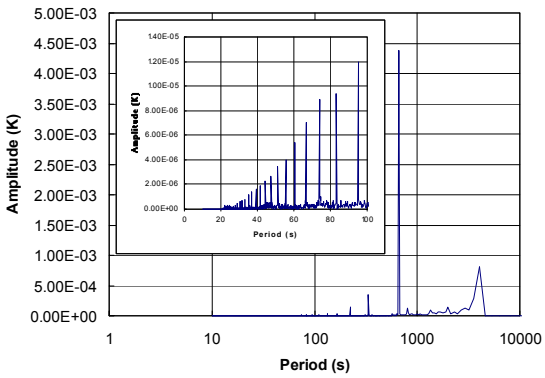

(b)

Figure 9-4. Same as in Figure 9-1 for the 100 GHz front-end radiometers.

9.2 Case of 5-equal homogeneous compressors + 1 non-homogeneous compressor

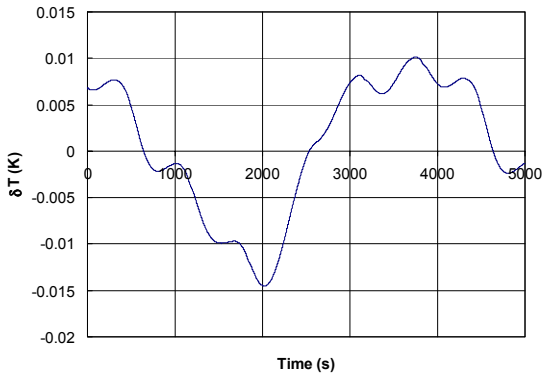

(a)

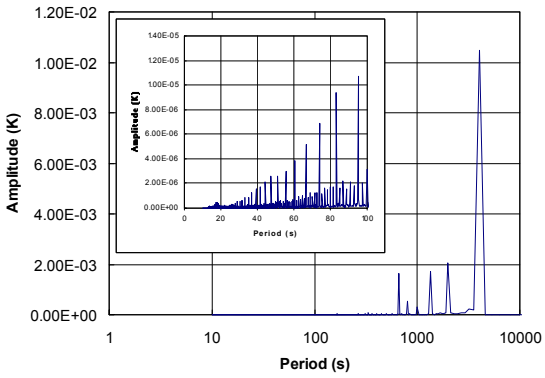

(b)

Figure 9-5. Expected temperature oscillation at the 30 GHz front-end radiometers considering a Sorption

Cooler characterised by 5 equal compressors with homogeneous beds and 1 compressor bed with non-homogeneous hydride distribution; (a) oscillation in time domain, (b) Fourier transform

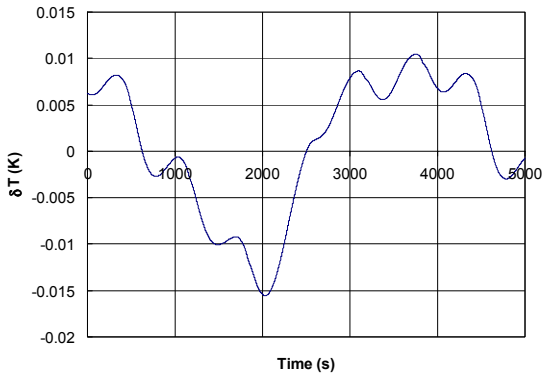

(a)

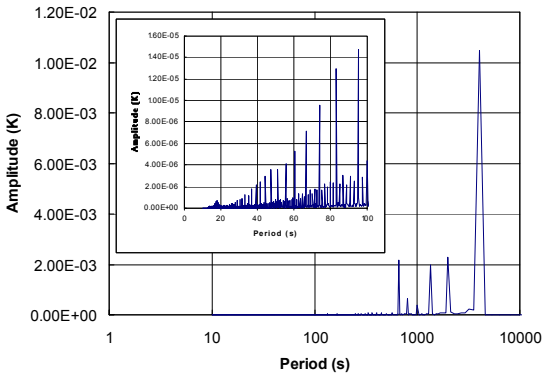

(b)

Figure 9-6. Same as in Figure 9-5 for the 44 GHz front-end radiometers.

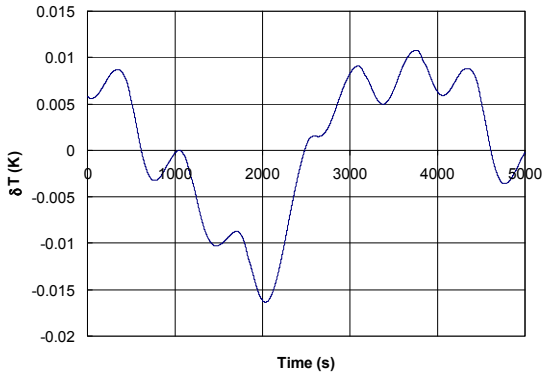

(a)

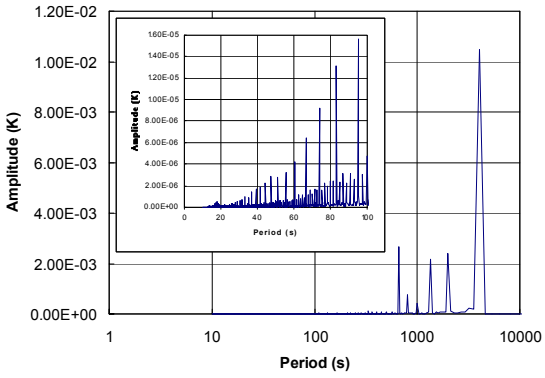

(b)

Figure 9-7. Same as in Figure 9-5 for the 70 GHz front-end radiometers.

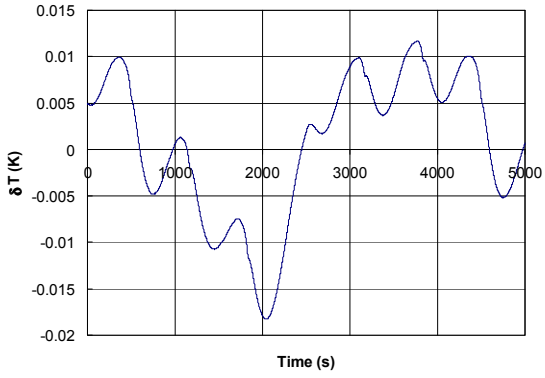

(a)

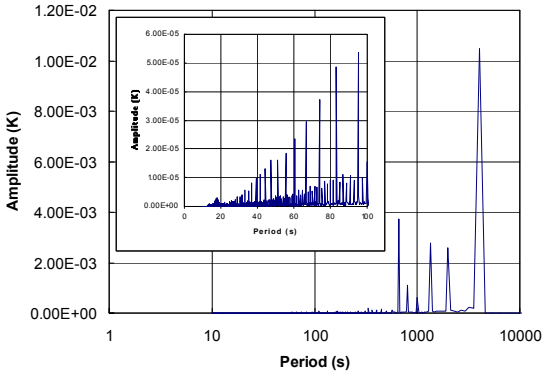

(b)

Figure 9-8. Same as in Figure 9-5 for the 100 GHz front-end radiometers.

9.3 Case of 3-equal homogeneous compressors + 3 non-homogeneous compressors

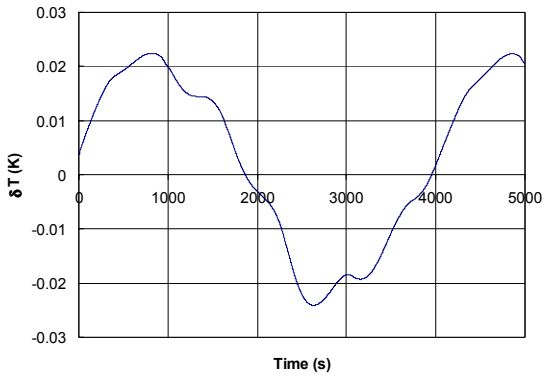

(a)

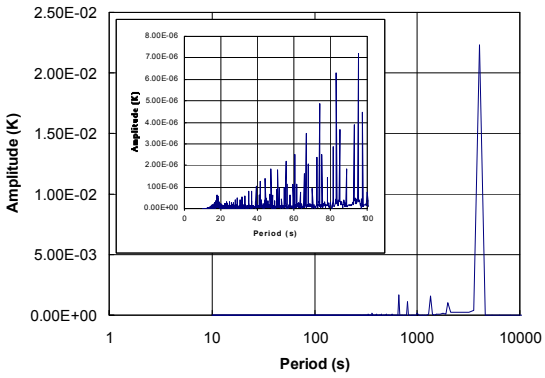

(b)

Figure 9-9. Expected temperature oscillation at the 30 GHz front-end radiometers considering a Sorption Cooler characterised by 5 equal compressors with homogeneous beds and 1 compressor bed with non-homogeneous hydride distribution; (a) oscillation in time domain, (b) Fourier transform

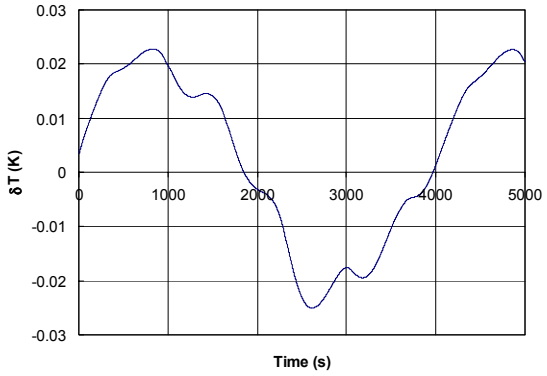

(a)

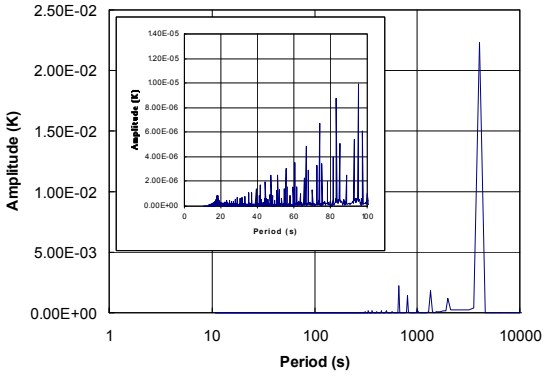

(b)

Figure 9-10. Same as in Figure 9-9 for the 44 GHz front-end radiometers.

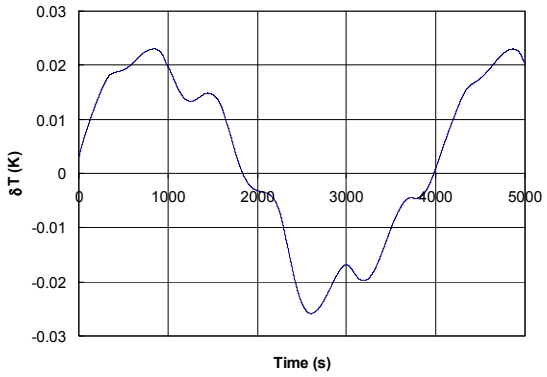

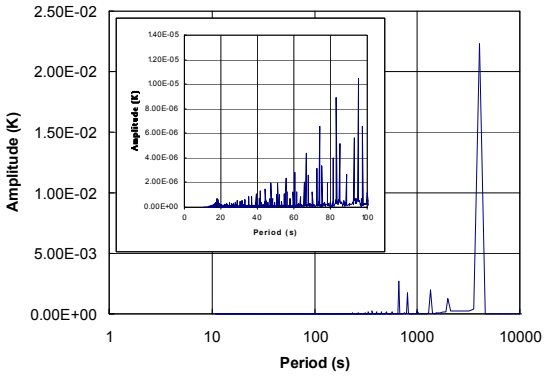

(a) (b)

Figure 9-11. Same as in Figure 9-9 for the 70 GHz front-end radiometers.

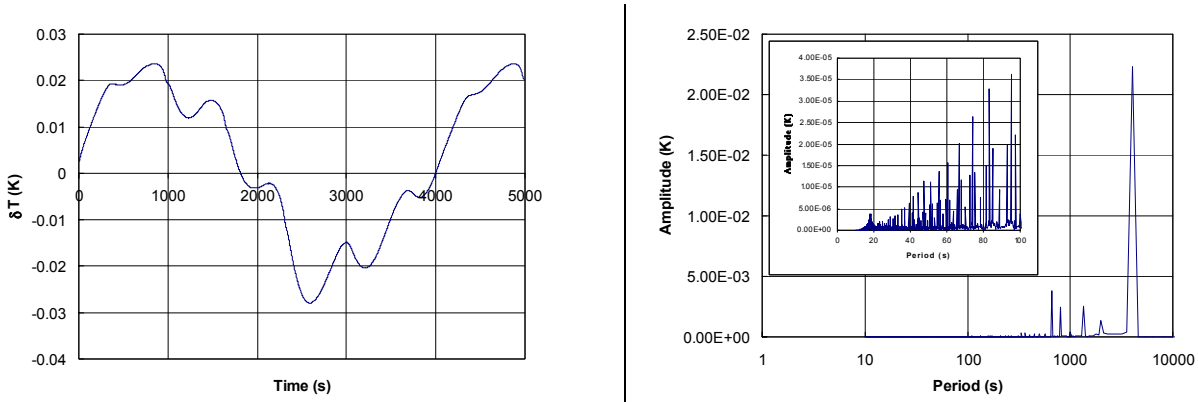

(a) (b)

Figure 9-12. Same as in Figure 9-9 for the 100 GHz front-end radiometers